Ko *et al. Nanoscale Research Letters* (2022) 17:106
https://doi.org/10.1186/s11671-022-03741-0

Nanoscale Research Letters

RESEARCH Open Access

Passivation and Interlayer Effect of $Zr(i\text{-}PrO)_4$ on Green $CuGaS_2/ZnS/Zr(i\text{-}PrO)_4@Al_2O_3$ and Red $CuInS_2/ZnS/Zr(i\text{-}PrO)_4@Al_2O_3$ QD Hybrid Powders

Minji Ko, Soyeon Yoon, Yun Jae Eo, Keyong Nam Lee and Young Rag Do*

Abstract

Broadband emissive I–III–VI quantum dots (QDs) are synthesized as efficient and stable I–III–VI QDs to be used as eco-friendly luminescent materials in various applications. Here, we introduce the additional passivation of zirconium isopropoxide ($Zr(i\text{-}PrO)_4$) to improve the optical properties and environmental stability of green-emitting $CuGaS_2/ZnS$ (G-CGS/ZnS) and red-emitting $CuInS_2/ZnS$ (R-CIS/ZnS) QDs. The photoluminescence quantum yield (PLQY) of both resultant $Zr(i\text{-}PrO)_4$-coated G-CGS/ZnS and R-CIS/ZnS QDs reaches similar values of ~ 95%. In addition, the photostability and thermal-stability of G-CGS/ZnS/$Zr(i\text{-}PrO)_4$ and R-CIS/ZnS/$Zr(i\text{-}PrO)_4$ QDs are improved by reducing the ligand loss via encapsulation of the ligand-coated QD surface with $Zr(i\text{-}PrO)_4$. It is also proved that the $Zr(i\text{-}PrO)_4$-passivated interlayer mitigates the further degradation of I-III-V QDs from ligand loss even under harsh conditions during additional hydrolysis reaction of aluminum tri-sec-butoxide ($Al(sec\text{-}BuO)_3$), forming easy-to-handle G-CGS/ZnS and R-CIS/ZnS QD-embedded Al_2O_3 powders. Therefore, the introduction of a $Zr(i\text{-}PrO)_4$ complex layer potentially provides a strong interlayer to mitigate degradation of I–III–VI QD-embedded Al_2O_3 hybrid powders as well as passivation layer for protecting I–III–VI QD.

Keywords: I–III–VI quantum dots, Hydrolysis, Surface passivation, Stability, QD doping

Introduction

Recently, eco-friendly I–III–VI quantum dots (QDs) have been studied intensively in an effort to prepare broadband emissive QD materials for bio-applications and for lighting with high color rendering index (CRI) (> 90) [1–5]. However, QD emission characteristics and material stability levels remain inferior to those of environmentally toxic Cd-based II-VI chalcogenide QDs. Hence, improved photoluminescence quantum yields (PLQYs) and enhanced material stability of I–III–VI QDs are required for their application to various lighting and bio-applications. To date, the record high PLQYs of I–III–VI QDs have already exceeded 90% in the solution form of QD colloids dispersed in an organic solvent [6, 7]. Occasionally, as-prepared I–III–VI QD solutions are not sufficiently stable to be applied to lighting devices or bio-applications due to the limited UV and thermal stability of I–III–VI QDs during the transforming process of QD powders and post-coating process of oxide encapsulants [8, 9].

Surface passivation of QDs is a facile process that can be utilized during the synthesis of I–III–VI QDs for green and red (GR) color-converting materials in white LEDs [10–16]. It is well known that the ligand passivation of QDs can form a protective layer to improve the material stability of QDs against environmental attacks, such as those by light, humidity, and operation heat [17–20]. However, it is a critical issue that organic ligands quickly

*Correspondence: yrdo@kookmin.ac.kr
Department of Chemistry, Kookmin University, Seoul 02707, Republic of Korea

© The Author(s) 2022. **Open Access** This article is licensed under a Creative Commons Attribution 4.0 International License, which permits use, sharing, adaptation, distribution and reproduction in any medium or format, as long as you give appropriate credit to the original author(s) and the source, provide a link to the Creative Commons licence, and indicate if changes were made. The images or other third party material in this article are included in the article's Creative Commons licence, unless indicated otherwise in a credit line to the material. If material is not included in the article's Creative Commons licence and your intended use is not permitted by statutory regulation or exceeds the permitted use, you will need to obtain permission directly from the copyright holder. To view a copy of this licence, visit http://creativecommons.org/licenses/by/4.0/.

degrade under various environmental conditions, such as high temperature, intensive UV irradiation, and high humidity. To solve this issue, various additional surface passivation or encapsulation processes were introduced at defects sites on the QD surface to reduce ligand loss. Among them, the mitigation band gap between the core and shell structure is the one of the ways to enhance surface passivation [6, 12]. Introduction of a polymer matrix such as polyvinylpyrrolidone (PVP), polymethylmethacrylate (PMMA), and polyvinyl alcohol (PVA) is an additional way to improve surface passivation [13, 21]. Additional passivation was performed to maintain the high PLQY in the QD solution form under various environmental conditions [21–23]. Furthermore, metal–organic frameworks (MOFs) were developed as a method to enhance the stability of QDs [24]. As previously reported, the hydrolysis reaction of metal alkoxide precursors is a well-known and facile encapsulation process to embed QDs into an inorganic–organic matrix powder [22, 23, 25]. In most hydrolysis reactions of metal alkoxides, acid and base catalysts are used to accelerate hydrolysis reactions, and a small amount of water is necessary to complete the hydrolysis reactions. Unfortunately, both acid/based catalysts and water can cause photoluminescent quantum yield (PLQY) degradation of nearly all types of QDs during hydrolysis [26, 27]. Nonetheless, certain easy synthetic processes, including the Stöbber reaction [28–31] can enable most hydrolysis reactions to produce oxide encapsulated QD powders via inorganic polymerization and gelation and hydrolysis processes [11, 32–36]. Meanwhile, Prof. Yang's group introduced a Zr-alkoxide that can be used as secondary passivation material for narrow-band InP/ZnSeS/ZnS-based QDs to improve environmental stability [37, 38]. However, there have been no detailed reports on secondary passivation effects of metal alkoxides to mitigate the degradation of eco-friendly I–III–VI QDs and I–III–VI QD-embedded oxide powders during simple hydrolysis reaction.

In this study, we enhanced the stability of both G-CGS/ZnS and R-CIS/ZnS QDs in two steps involving a secondary ligand and aluminum tri-sec-butoxide (Al(sec-BuO)$_3$) [14, 22, 25]. Due to the introduction of zirconium isopropoxide (Zr(i-PrO)$_4$) as a secondary ligand, the stability of both G-CGS/ZnS and R-CIS/ZnS QDs primarily increased. We further introduced Al(sec-BuO)$_3$ as an effective precursor for use in fast hydrolysis reactions without requiring acid/base catalysts or water. So, G-CGS/ZnS and R-CIS/ZnS QD-embedded Al_2O_3 hybrid powders were synthesized by fast hydrolysis reaction with a mixture solution of Al(sec-BuO)$_3$ and Zr(i-PrO)$_4$-decorated I–III–VI QDs in toluene. We also analyzed the degree to which Zr(i-PrO)$_4$ secondary ligands protect degradation of I–III–VI QDs during hydrolysis reaction. Finally, the passivation effect of Zr(i-PrO)$_4$ secondary ligand was investigated by comparing the optical properties of two down-converted white LEDs (DC-WLEDs), which include G-CGS/ZnS and R-CIS/ZnS QDs@Al_2O_3 QD hybrid powders and G-CGS/ZnS and R-CIS/ZnS/Zr(i-PrO)$_4$@Al_2O_3 QD hybrid powders. We confirmed that secondary ligand passivation such as a coating of Zr(i-PrO)$_4$ not only improves the environmental stability of the eco-friendly I–III–VI QDs itself, but also mitigates further degradation of I–III–VI QDs during additional inorganic coating and device fabrication processes [25, 39].

Experimental

Materials

Copper(I) iodide (CuI, 99.999%, Aldrich), gallium(III) iodide (GaI_3, 99.99%, Aldrich), indium(III) acetate ($In(ac)_3$, 99.99%, Aldrich), sulfur (S, 99.98%, Aldrich), zinc acetate dihydrate ($Zn(ac_2$, reagent grade, Aldrich), zinc stearate (10 − 12% Zn basis, Aldrich), zirconium(IV) propoxide solution (Zr(i-PrO)$_4$, 70 wt% in 1-propanol, Aldrich), (oleylamine (OLA, 70%, Aldrich), 1-dodecanethiol (DDT, 98%, Aldrich), oleic acid (OA, 90%, Aldrich), 1-octadecene (ODE, 90%, Aldrich), aluminum-tri-sec-butoxide (Al(O-sec-Bu)$_3$, 97%, Aldrich), UV-curable polymer (NOA 61, Norland Products, Inc.) and cup-type of InGaN LED (λ_{max} = 450 nm, Dongbu LED Co. Ltd., Inc.) were utilized.

Synthesis of Red CIS/ZnS and CIS/ZnS/Zr(i-PrO)$_4$ QDs

To synthesize the CIS/ZnS QDs, 0.125 mmol of CuI, 0.5 mmol of $In(ac)_3$, 0.5 mL of DDT and 5 mL of OLA were loaded into a three-necked flask. The loaded precursors were supplied with N_2 gas for 15 min at room temperature. After N_2 purging, 0.2 mmol of sulfur dissolved in 2 mL of ODE was rapidly injected into the three-necked flask at 140 °C for three minutes. For the first shelling process, we injected 8 mL of a prepared Zn stock solution consisting of 5.3 mmol of $Zn(ac)_3$ dissolved in 2.7 mL of ODE and 5.3 mL of OA at 240 °C for 30 min. For the second shelling process, 8 mL of the prepared Zn stock solution (5.3 mmol of zinc stearate) dissolved in 2.7 mL of DDT and 5.3 mL of ODE was loaded into the reaction pot at 240 °C for two hours. For the in-situ-treatment of Zr(i-PrO)$_4$ with the synthesized CIS/ZnS QDs, 1 mL of the Zr(i-PrO)$_4$ was injected into the reaction solution at 240 °C for 30 min. The synthesized QD solution was centrifuged for purification and dispersed in hexane.

Synthesis of Green CGS/ZnS and CGS/ZnS/Zr(i-PrO)$_4$ QDs

To synthesize the CGS/ZnS QDs, 0.125 mmol of CuI, 0.75 mmol of GaI_3, 1.0 mmol of S, 1.5 mL of DDT and

5 mL of OLA were loaded into a three-necked flask. The loaded precursors were purged with N_2 gas for 15 min at room temperature. The reaction flask was quickly heated to 240 °C and reacted for 5 min to grow the core. For the shelling process, we utilized three sequential steps. For the first shelling process, we injected 12 mL of a prepared Zn stock solution consisting of 8 mmol of $Zn(ac)_3$ dissolved in 4 mL of ODE and 8 mL of OA at 240 °C for an hour. Second, we injected 8 mL of a prepared Zn stock solution consisting of 4 mmol of $Zn(ac)_3$ dissolved in 2 mL of ODE, 2 mL of DDT and 4 mL of OA at 240 °C for 30 min. Lastly, we injected a Zn stock solution consisting of 4 mmol of Zinc stearate dissolved in 4 mL of DDT and 4 mL of ODE at 250 °C for two hours. 1 mL of $Zr(i\text{-}PrO)_4$ was injected into the growth solution at 250 °C for 30 min to initiate in-situ-treatment of $Zr(i\text{-}PrO)_4$ on the surface of synthesized CGS/ZnS QDs. The synthesized QD solution was dispersed in hexane after the purification.

Fabrication of Al_2O_3 Encapsulated Red and Green QD Hybrid Powders

The purified QDs were diluted to an optical density of 1.4 (at 450 nm). We prepared a 30 wt% $Al(O\text{-}sec\text{-}Bu)_3$ solution that dissolved in toluene. We prepared Al-QD stock solution in which the diluted QDs were added to the prepared 30 wt% $Al(O\text{-}sec\text{-}Bu)_3$ solution at a volume ratio of 2:1. Al_2O_3 encapsulated red and green QD hybrid powders were fabricated through ex-situ hydrolysis reaction of prepared Al-QD stock solution under ambient moisture at room temperature.

Fabrication of Green–Red QD-Embedded Al_2O_3 Hybrid Powder-Based Single-Package WLED

The obtained green and red QD-embedded Al_2O_3 powders were mixed with the UV-curable binder NOA 61 to fabricate a single-package WLED. An appropriate amount of green and red QD powder/NOA 61 mixture was dropped onto a cup-type InGaN blue LED, which was used as an excitation source. The InGaN blue LED to which green and red QD powder/NOA 61 was then exposed to UV light (at 365 nm) for 30 min to harden the green and red QD/NOA 61 mixture. The obtained green–red QD-embedded Al_2O_3 hybrid powder-based single-package was realized as a 6,500 K white down-converted LED at an applied current of 60 mA.

Characterization

The absorbance and PL emission spectra of the synthesized red CIS/ZnS, CIS/ZnS/$Zr(i\text{-}PrO)_4$ and green CGS/ZnS, CGS/ZnS/$Zr(i\text{-}PrO)_4$ QDs were measured with a UV–visible spectrometer (Lambda 365, Perkin Elmer) and a PL spectrophotometer with an Xe lamp (Darsa, PSI Trading), respectively. PLQY values of the QDs were calculated by comparison with standard rhodamine 6G (QY = 95% in ethanol). The crystal phase of the obtained QDs was characterized by X-ray diffractometry (XRD; D/MAX-2500 V, Rigaku). A scanning electron microscope (SEM; JSM-7610F, JEOL, Ltd.) and a transmission electron microscope (TEM; JEM-F200, JEOL, Ltd.) with energy-dispersive X-ray spectroscopy (EDS) were utilized to analyze the size, morphology and crystal structure, and to perform elemental analysis of the obtained red CIS/ZnS, CIS/ZnS/$Zr(i\text{-}PrO)_4$ and green CGS/ZnS, CGS/ZnS/$Zr(i\text{-}PrO)_4$ QDs and Al_2O_3 encapsulated QD hybrid powders. To analyze the functional groups of ligands in the obtained red CIS/ZnS, CIS/ZnS/$Zr(i\text{-}PrO)_4$ and green CGS/ZnS, CGS/ZnS/$Zr(i\text{-}PrO)_4$ QDs, Fourier transform infrared (FT-IR) measurement with an IR spectrophotometer (Nicolet iS50, Thermo Fisher Scientific) was conducted. The EL emission spectra of the fabricated Al_2O_3 encapsulated green and red QD hybrid powders single-package down-converted WLEDs were measured using a spectrophotometer (Darsapro-5000, PSI Co. Ltd.).

Results and Discussion

We synthesized both G-CGS/ZnS and R-CIS/ZnS QDs using a multi-step hot-injection method according to synthetic processes reported in our previous studies (Fig. 1). Both G-CGS/ZnS/$Zr(i\text{-}PrO)_4$ QDs and R-CIS/ZnS/$Zr(i\text{-}PrO)_4$ QDs were obtained by in-situ treatment with $Zr(i\text{-}PrO)_4$ after synthesizing G-CGS/ZnS and R-CIS/ZnS QDs, as previously reported [2, 3].

The X-ray diffraction (XRD) patterns of the two green QDs of pristine CGS/ZnS and CGS/ZnS/$Zr(i\text{-}PrO)_4$ and two red QDs of pristine CIS/ZnS and CIS/ZnS/$Zr(i\text{-}PrO)_4$ are shown in Fig. 2a, b, respectively. The peak shift of the main diffraction peaks of $CuGaS_2$ and $CuInS_2$ to higher values of 2θ and the merged main peaks of $CuGaS_2$ (or $CuInS_2$) and ZnS diffraction peaks indicate that alloyed structures were formed in these I-I I–III–VI core/ZnS shell QDs, which matches with the XRD patterns in previous publications [3, 6]. The reduced peak intensity and unchanged peak positions of QDs treated with $Zr(i\text{-}PrO)_4$ molecules are presumably attributable to the attenuation of diffracted XRD patterns by the $Zr(i\text{-}PrO)_4$ molecules successfully screened on the ZnS surface. The XRD intensity of larger green QDs is slightly reduced, but that of the smaller red QDs is slightly more reduced by the different screening effects of the $Zr(i\text{-}PrO)_4$ coating. Figure 2c–f presents transmission electron microscopy (TEM) images of two green and two red pristine and $Zr(i\text{-}PrO)_4$-decorated QDs. These images indicate that the average sizes of both the G- and R-emitting QDs are little changed after the $Zr(i\text{-}PrO)_4$ complexing

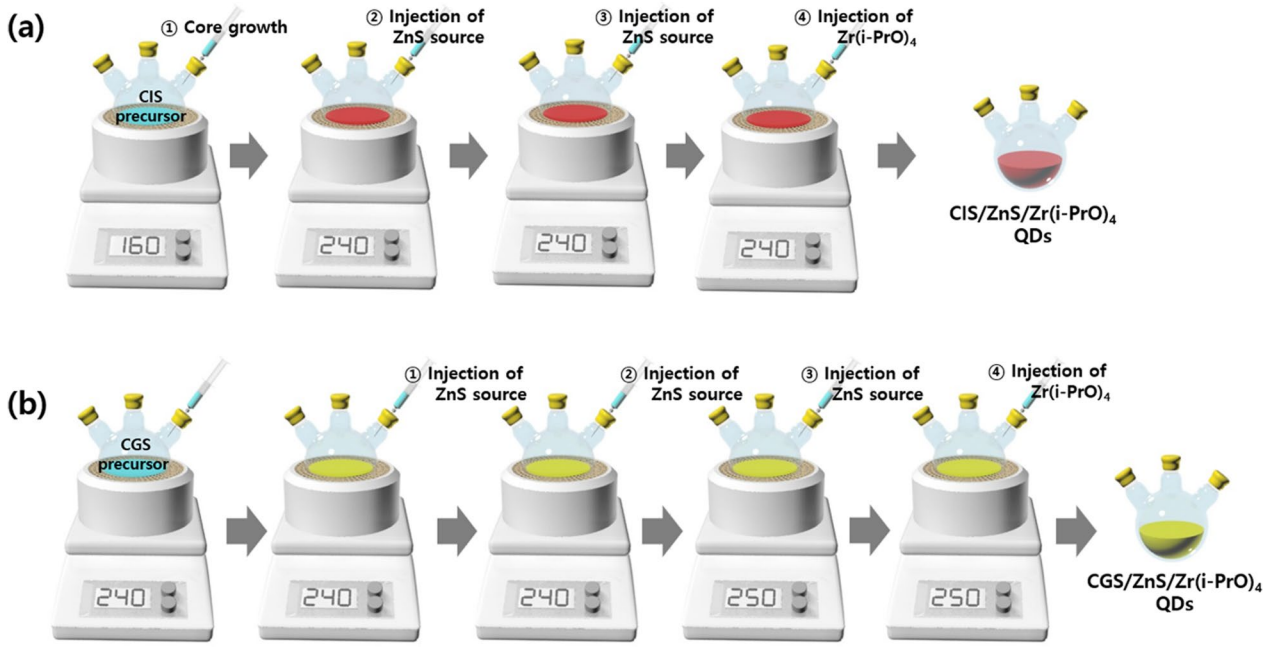

Fig. 1 Schematic diagram of both **a** red CIS/ZnS and **b** green CGS/ZnS QDs using multi-step hot-injection method

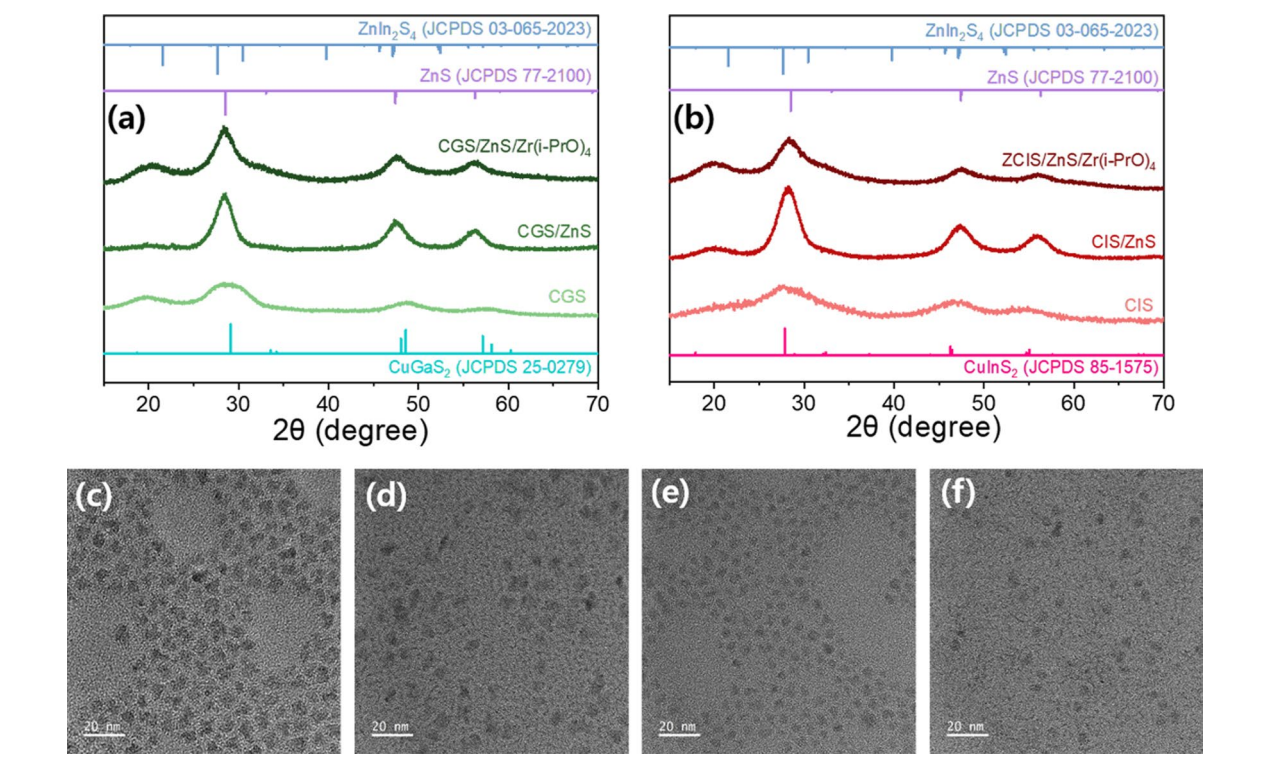

Fig. 2 XRD patterns of **a** green QDs of CGS, CGS/ZnS and CGS/ZnS/Zr(i-PrO)$_4$ and **b** red QDs of CIS, CIS/ZnS and CIS/ZnS/Zr(i-PrO)$_4$. TEM images of green QDs of: **c** CGS/ZnS and **d** CGS/ZnS/Zr(i-PrO)$_4$; red QDs of **e** CIS/ZnS and **d** CIS/ZnS/Zr(i-PrO)$_4$

process on the surface of both the G and R I–III–VI QDs (Additional file 1: Fig. S1).

The TEM images also indicate that two G and two R QDs are suitably grown with single crystal-like nanoparticles. The TEM results imply that the coated Zr(i-PrO)$_4$ complexes cannot be transformed into thick ZrO_2 oxide overcoating via thermal decomposition even at high reaction temperature of 240 ~ 250 °C. XPS analyses were performed to compare two types of QDs, such as pristine and Zr(i-PrO)$_4$-decorated G-CGS/ZnS and R-CIS/ZnS QDs. In the high-resolution XPS peaks in Fig. 3, shoulder peaks of the O 1s signals can be distinctly seen after each Zr(i-PrO)$_4$ coating process in both G-CGS/ZnS/Zr(i-PrO)$_4$ and R-CIS/ZnS/Zr(i-PrO)$_4$ QDs due to the Zr-O bonds from metal alkoxide liganded QDs. As reported in previous publications [23, 38], the O 1s peak of unreacted QDs is due to oxygen species from carboxylate QD ligands and atmospheric gaseous oxygen species adsorbed on the QD surface. Otherwise, the O 1s peaks of complexed Zr(i-PrO)$_4$-QDs can deconvolute into two sub-spectra. The two peaks of O 1s from the Zr(i-PrO)$_4$-coated GR QDs are centered at binding energies of 531.7 and 530.4 eV, respectively [38]. The first 531.7 eV peak of both GR samples is the same as that in the uncoated alloy-core/shell QDs. The second peak is typically an oxygen peak from the Zr–O bond of Zr(i-PrO)$_4$. All G and R QD samples show nearly constant peaks of Cu 2d, Ga 2d, Zn 2p, and S $2p_{3/2}$ for G QDs and Cu 2d, In 3d, and Zn 2p, S $2p_{3/2}$ for R QDs, respectively [37, 38].

Figure 4a, d shows the FT-IR spectra of the G and R-emitting pristine and Zr(PrO)$_4$-decorated QD solutions. The two pristine G and R QD samples commonly show strong bands at 2920, 2850, 1550, and 1450 cm^{-1}, which are assigned to $-CH_2$, $-CH_3$ stretching, COO– antisymmetric stretching mode, and COO– symmetric stretching mode, respectively [23, 37]. These are attributed to aliphatic surface ligands, such as stearate, oleate, and dodecyl and carboxylate groups of fatty acid bonded on the QD surface. As can be seen in the FT-IR spectra, the C–H and COO– stretching modes of the ligand-attached QD solution samples indicate that the ligand

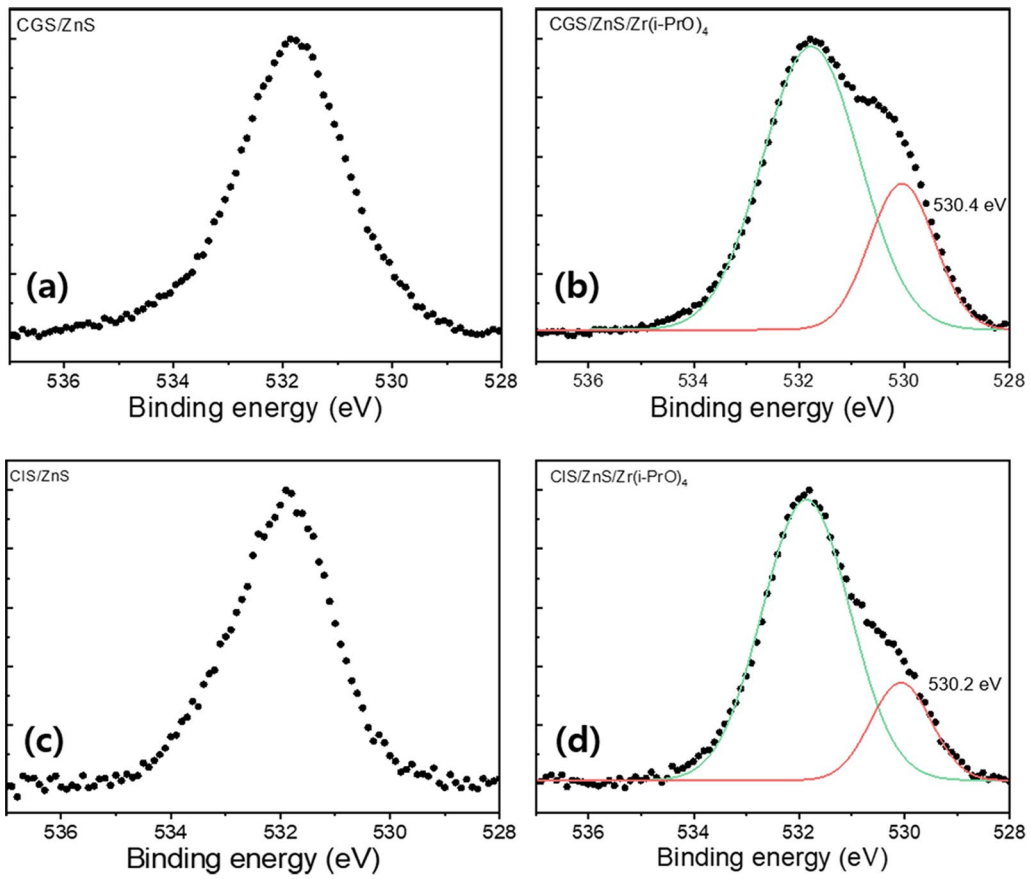

Fig. 3 Partial XPS survey results of O component peaks of green **a** CGS/ZnS and **b** CGS/ZnS/Zr(i-PrO)$_4$ QDs; and red **c** CIS/ZnS and **d** CIS/ZnS/Zr(i-PrO)$_4$ QDs. In the XPS spectra, ZrO_2 (red line) peak is deconvoluted from the original O spectra (black line)

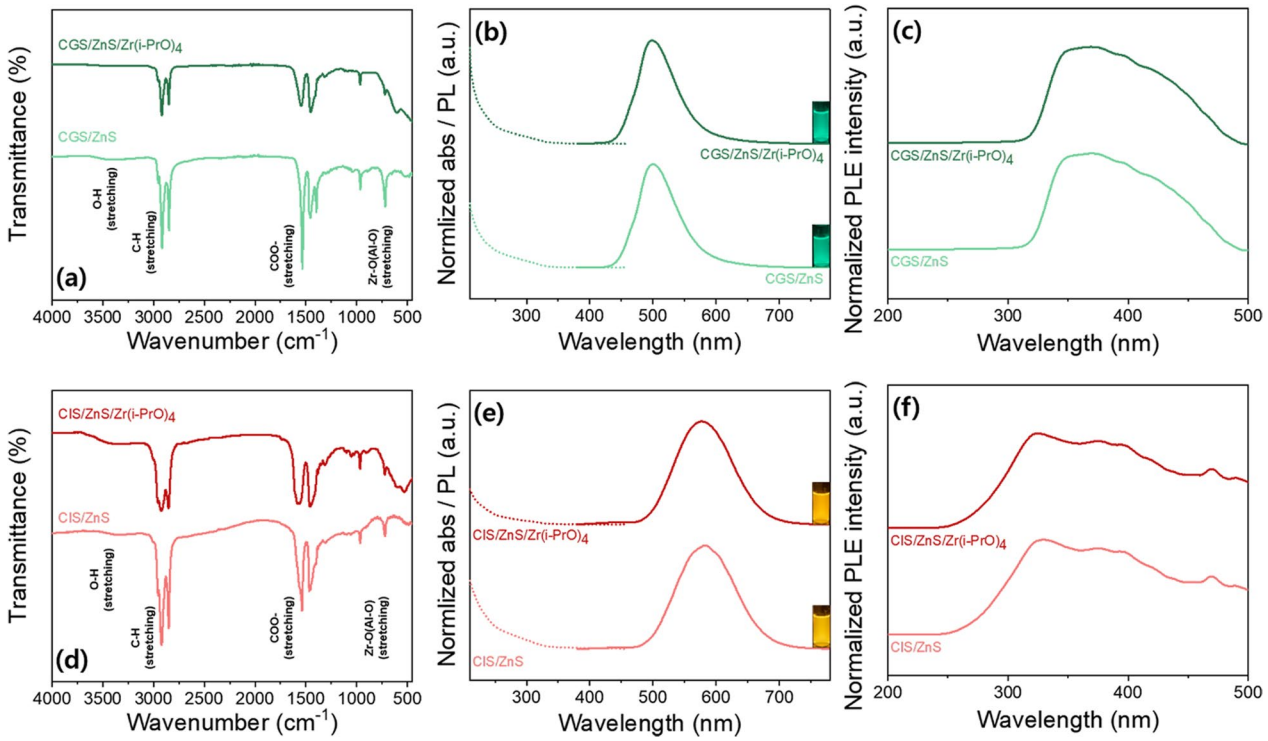

Fig. 4 FT-IR spectra of **a** green pristine CGS/ZnS and CGS/ZnS/Zr(i-PrO)$_4$ and **d** red pristine CIS/ZnS and CIS/ZnS/Zr(i-PrO)$_4$ QD solutions. PL emission spectra, absorbance, and photographs of emitting solutions (inset) of **b** green pristine CGS/ZnS, CGS/ZnS/Zr(i-PrO)$_4$ and **e** red pristine CIS/ZnS and CIS/ZnS/Zr(i-PrO)$_4$ QD solutions. **c** PLE spectra of green pristine CGS/ZnS, CGS/ZnS/Zr(i-PrO)$_4$ and **f** red pristine CIS/ZnS and CIS/ZnS/Zr(i-PrO)$_4$ QD solutions

signals of the pristine QDs are slightly reduced by the screening effect or the ligand detachment effect of Zr(i-PrO)$_4$. The stretching mode of the ligand is still strong, so the ligands are mostly attached to the surface of the QDs, despite the alkoxide coating. The distinct band at 500 cm^{-1} can be associated with the Zr–O stretching band of Zr(i-PrO)$_4$ molecules [37]. These results also prove indirectly the suitable complexing on the ZnS surface of QDs with metal alkoxide forms.

Changes in normalized PL, PL excitation (PLE), and absorption spectra of solution forms of pristine QDs and G-CGS/ZnS/Zr(i-PrO)$_4$ and R-CIS/ZnS/Zr(i-PrO)$_4$ QDs are shown in Fig. 4b, c and Fig. 4e, f. The peak position and full-width at half maximum (FWHM) of the PL emission spectra of G-CGS/ZnS and R-CIS/ZnS QDs are almost unchanged after sequential coating of Zr(i-PrO)$_4$ alkoxides. Small differences of the PLE and absorption spectra between the two solution-typed QD samples can be thought to have arisen from the additional absorption of complexing molecules of Zr(i-PrO)$_4$ after the Zr(i-PrO)$_4$ coating process. Table 1 summarizes the detailed optical properties of the two GR pristine QDs and two Zr(i-PrO)$_4$ complexed QDs. As previously reported, the PLQYs of the Zr(i-PrO)$_4$ complexed QDs are slightly higher than or similar to those of pristine QDs [38]. As a result, the PLQYs of both resultant G-CGS/ZnS/Zr(i-PrO)$_4$ and R-CIS/ZnS/Zr(i-PrO)$_4$ QDs reach similar values of ~ 95%. It can be seen that the additional surface passivating process with Zr(PrO)$_4$ hardly changed the optical properties, such as peak wavelength, FWHM, and CIE color coordinates of both G-CGS/ZnS and R-CIS/ZnS QDs, as summarized in Table 1. These materials also emit similar bright green and orange-red color before and after Zr(PrO)$_4$ complexation, as shown in the insets

Table 1 Detailed optical properties of four QD solutions (CGS/ZnS, CGS/ZnS/Zr(i-PrO)$_4$, CIS/ZnS and CIS/ZnS/Zr(i-PrO)$_4$)

Sample	Color coordinates		Peak wavelength (nm)	FWHM (nm)	PLQY (%)
	CIEx	CIEy			
CGS/ZnS	0.236	0.479	499	71	93
CGS/ZnS/Zr(i-PrO)$_4$	0.229	0.472	498	70	95
CIS/ZnS	0.521	0.464	582	108	94
CIS/ZnS/Zr(i-PrO)$_4$	0.511	0.470	578	105	95

of Fig. 4b, e. Although it has not been fully established how much Zr(i-PrO)$_4$ chemically decorates the surface of QDs, PL spectra results show that these complexing processes preserve the PL properties of pristine GR QD solutions.

Next, to compare the stability of pristine and Zr(i-PrO)$_4$-complexed G-CGS/ZnS and R-CIS/ZnS QDs, stability tests were performed in the colloidal solution form. For the solution test, pristine and Zr(i-PrO)$_4$-complexed G-CGS/ZnS and R-CIS/ZnS QD colloids were dispersed in ODE and their colloidal solutions were placed under continuous UV (365 nm) irradiation or on a hot plate at 150 °C for prolonged periods of time. As shown in Fig. 5a, b, largely increased stability values of both G and R QDs were observed under UV irradiation, clearly indicating that the passivating effect of the Zr(i-PrO)$_4$-complex is strongly effective on the surfaces of both ZnS-shelled G-CGS and R-CIS QDs. Pristine G-CGS/ZnS and R-CIS/ZnS QDs retained values of only 19% and 66% of their original PLQYs after 12 h and 24 h of UV irradiation, respectively.

QD precipitations of both G-CGS/ZnS and R-CIS/ZnS QDs were observed clearly under long-term exposure to UV irradiation, indicating the desorption of liable ligands and flocculation of both G-CGS/ZnS and R-CIS/ZnS QDs by the change in surface hydrophilicity through photochemical reactions. Meanwhile, both Zr(i-PrO)$_4$-complexed G-CGS/ZnS and R-CIS/ZnS QDs showed moderate PLQY drops for up to 6 h, retaining ~ 50% of the initial value for green QDs after 12 h and ~ 92% for red QDs after 24 h. The improved photo-stability of Zr(i-PrO)$_4$-coated G-CGS/ZnS and R-CIS/ZnS QDs indicates that Zr(i-PrO)$_4$-complexed on the surface of QDs suppresses the desorption of ligands from the surfaces of both G-CGS/ZnS and R-CIS/ZnS QDs. The mixture of Zr(i-PrO)$_4$ and G-CGS/ZnS and R-CIS/ZnS QDs showed a trend of photo-stability as a function of UV irradiation similar to that of pristine G-CGS/ZnS and R-CIS/ZnS QDs. These trends suggest that non-complexed molecules did not contribute to the surface passivation and that Zr(i-PrO)$_4$ was complexed on the surface of QDs; these results match well with the results of the previous report [37]. The thermal stability performances of both Zr(i-PrO)$_4$-complexed G-CGS/ZnS and R-CIS/ZnS QDs were assessed by analyzing the degradation of PLQY of both G-CGS/ZnS and R-CIS/ZnS QDs in ODE solution

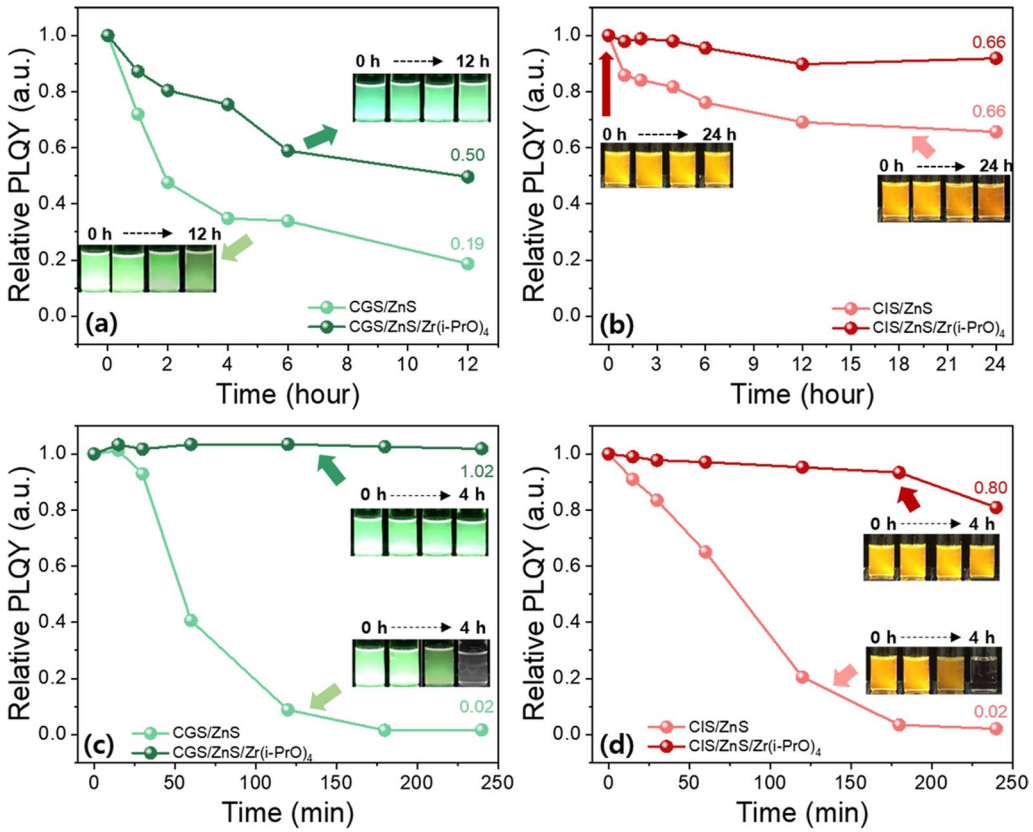

Fig. 5 Relative PLQY values from photostability tests of **a** green CGS/ZnS based solutions and **b** red CIS/ZnS based solutions under UV (365 nm) irradiation. Relative PLQY values from thermal stability tests of **c** green CGS/ZnS based solutions and **d** red CZS/ZnS based solutions under 150 °C

heated to 150 °C. Figure 5c, d shows temporal PLQY drops of pristine and $Zr(i\text{-}PrO)_4$-complexed G-CGS/ZnS and R-CIS/ZnS QDs under thermal degradation environment. Similar to the temporal degradation of PLQY under UV irradiation, the pristine GR QDs suffered from significant PLQY drops with progress of heating time. PLQY values of both G and R dropped to ~ 2% of the original values of G-CGS/ZnS and R-CIS/ZnS QDs, indicating that the thermal quenching of G-CGS/ZnS and R-CIS/ZnS QDs is due to oxidation and surface desorption of ligands. In contrast to the results of pristine QDs, ~ 102% and ~ 81% of initial PLQY values of both $Zr(PrO)_4$-complexed G-CGS/ZnS and R-CIS/ZnS QDs were maintained at 150 °C for the same period time. The slight shift of PL peaks of both pristine GR QDs explains the weakening phenomena of quantum confinement through the desorption of ligands and/or surface oxidation. Both temporal UV irradiation and heating test clearly suggested that the coating process of the $Zr(i\text{-}PrO)_4$-complex on the surface of both G-CGS/ZnS and R-CIS/ZnS QDs is an effective way to form a second passivation layer by reducing the photooxidation and desorption of ligands. To study the additional protection effect of the second $Zr(i\text{-}PrO)_4$ passivation interlayer during the oxide coating process, QD-embedded Al_2O_3 hybrid powders were synthesized by ex-situ hydrolysis reaction of $Al(sec\text{-}BuO)_3$ precursor using purified pristine and $Zr(i\text{-}PrO)_4$-complexed QD solutions under ambient moisture at room temperature, as shown in Fig. 6.

Figure 7 also shows that the XRD patterns of the final Al_2O_3 encapsulated G-CGS/ZnS and R-CIS/ZnS powder QDs remain in similar positions but their intensities are significantly reduced by the screening of Al_2O_3 coating materials. Moreover, the XRD peaks of Al_2O_3- and $Al_2O_3/Zr(i\text{-}PrO)_4$-coated G-CGS/ZnS and R-CIS/ZnS QDs are combined with an amorphous XRD hump of the

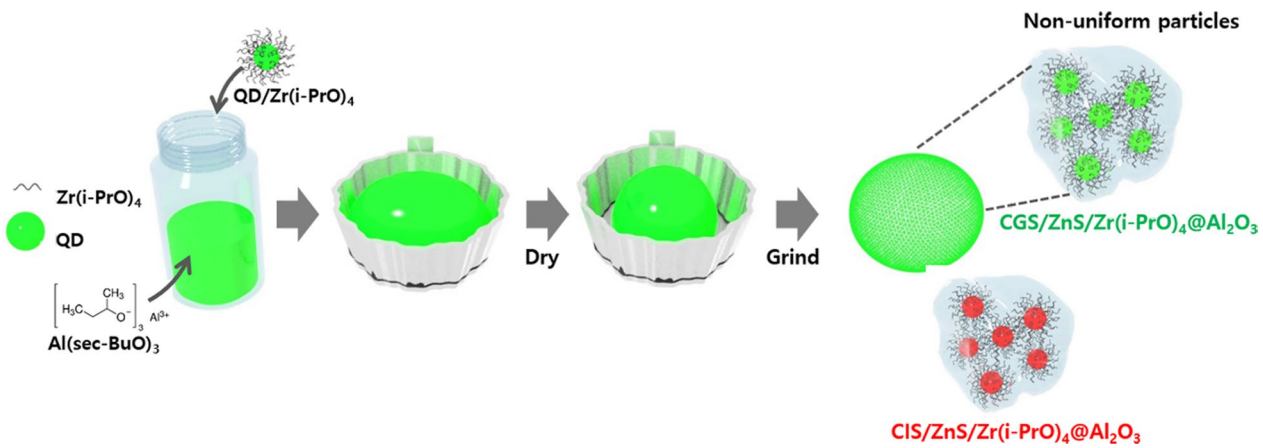

Fig. 6 Schematic diagram of ex-situ hydrolysis reaction of $Al(sec\text{-}BuO)_3$ precursor using purified pristine and $Zr(i\text{-}PrO)_4$-complexed QD solutions under ambient moisture at room temperature

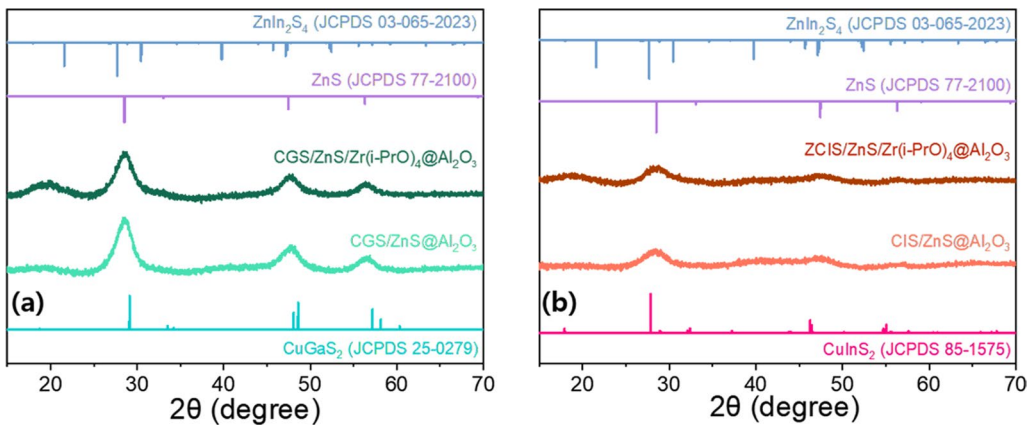

Fig. 7 XRD patterns of final Al_2O_3 encapsulated **a** green CGS/ZnS based and **b** red CIS/ZnS based powder QDs

Al_2O_3 matrix. Despite the hydrolysis reaction of Al(sec-BuO)$_3$ and the induced hydrolysis and complexation of Zr(i-PrO)$_4$ at room temperature, the crystallinity of the QDs is maintained.

TEM images of the final Al_2O_3- and Al_2O_3/Zr(i-PrO)$_4$-coated G-CGS/ZnS and R-CIS/ZnS QDs show that the QDs are well dispersed in the amorphous Al_2O_3 matrix after the quick hydrolysis reaction of Al(sec-BuO)$_3$ with ambient moisture and partially-induced hydrolysis reaction of Zr(i-PrO)$_4$ (Additional file 1: Fig. S2a–d). As shown in the SEM pictures and EDS data of Additional file 1: Fig. S2e–h and Fig. 3 ~ S4, the uniformly scattered Zr ions and uniformly distributed Al ions over the entire surface of the irregular-shaped micro-powders indicate that the I–III–VI QDs are coated with double alkoxide/oxides as doubly-passivated/encapsulated layer. Also, uniformly scattered Cu, Ga, In, Zn, and S ions indicate that the QDs are separately and uniformly embedded in the Al_2O_3 matrix, though their intensities are relatively low due to the screening effect of the Al_2O_3 matrix. As shown in the XPS data in Additional file 1: Fig. S5, the O 1s peaks from Al_2O_3-coated G-CGS/ZnS and R-CIS/ZnS QDs and Al_2O_3/Zr(i-PrO)$_4$-coated G-CGS/ZnS and R-CIS/ZnS QDs show two and three sub-spectra. However, in contrast to expectations, only one strong O 1s peak is shown after the Al_2O_3 encapsulating process. This means that the signals from the oxygen peaks of both pristine and Zr(i-PrO)$_4$-coated G-CGS/ZnS and R-CIS/ZnS QDs are screened by the thick encapsulant matrix of the Al_2O_3 powder matrix and then disappear. All XPS spectra indicate that the binding energy of the restrictive photoelectrons of each element from the QDs remains nearly unchanged even after Al_2O_3 encapsulant coating; however, due to the screening effect of additional metal alkoxide and oxide layers, these peak intensities somewhat decrease with increased number of sequential coatings of Zr(i-PrO)$_4$ and Al_2O_3. FT-IR measurements were performed on Al_2O_3- and Al_2O_3/Zr(i-PrO)$_4$-coated G-CGS/ZnS/ and R-CIS/ZnS QDs to further support the results of XPS analysis.

Figure 8a, b, indicates that all $-CH_2$, $-CH_3$, COO– antisymmetric, and COO– symmetric stretching modes are significantly reduced by the screening effect of Al_2O_3 encapsulant. The increased IR signals indicate that $-CH_2$

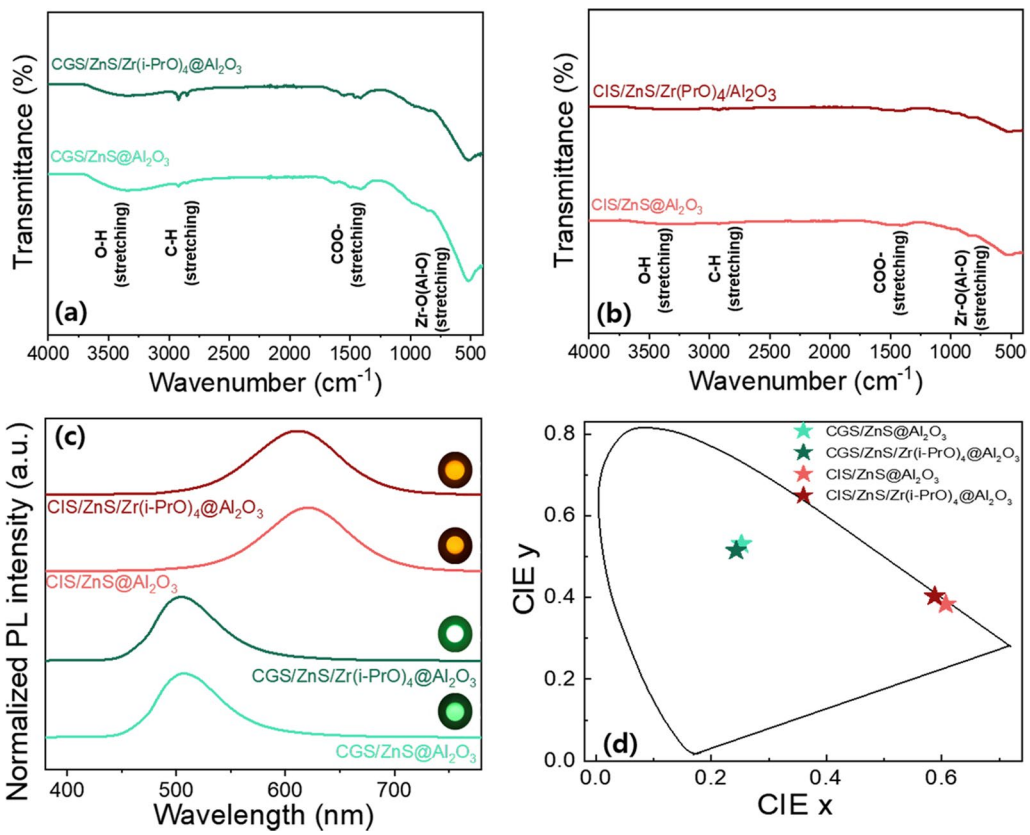

Fig. 8 FT-IR spectra of Al_2O_3 encapsulated **a** CGS/ZnS and **b** CIS/ZnS based powder QDs. **c** PL emission spectra and photographs of emitting powder QDs (inset) and **d** CIE color coordinates of Al_2O_3 encapsulated of CGS/ZnS based powder QDs and CIS/ZnS based powder QDs

and $-CH_3$ stretchings of the Al_2O_3/Zr(i-PrO)$_4$-coated G-CGS/ZnS and R-CIS/ZnS QD powders are stronger than those of the Al_2O_3-coated G-CGS/ZnS and R-CIS/ZnS QD powders, as shown Fig. 8a, b. This means that the passivation effect of the Zr(i-PrO)$_4$-complex keeps more ligands attached to the surface of the ZnS shell during the Al_2O_3 encapsulating process of the fast hydrolysis precursor of Al(sec-BuO)$_3$. As mentioned above, the distinct band at 500 cm^{-1} is associated with Zr-O stretching of the Zr(i-PrO)$_4$ complex [32]. However, these figures also show that FT-IR peaks from Al_2O_3-, Al_2O_3/Zr(i-PrO)$_4$-coated G-CGS/ZnS, and R-CIS/ZnS QDs consist of two bands from Al-O stretching (and/or Zr-O stretching), as well as common aliphatic and carboxy stretching bands. The different subpeak positions and shapes of the Al-O stretching bands between Al_2O_3-coated QDs and Al_2O_3/Zr(i-PrO)$_4$-coated QDs support the idea that the Al-O stretching band can screen the Zr-O stretching bands in Al_2O_3/Zr(i-PrO)$_4$-coated QD powders. Therefore, even if the complexing molecules of Zr(i-PrO)$_4$-coated QDs can be partially transformed by induced hydrolysis into oxide-layer encapsulated QDs, it can be assumed that the final encapsulated/passivated QDs can be expressed as Al_2O_3/Zr(i-PrO)$_4$-coated G-CGS/ZnS and R-CIS/ZnS QDs during the fast and strong hydrolysis reaction of the reactive Al(sec-BuO)$_3$ precursor. To compare the effects of inner Zr(i-PrO)$_4$ coating produced via complexation or partially-induced hydrolysis on PLQY values and stability of G-CGS/ZnS@Al_2O_3 and R-CIS/ZnS QDs@Al_2O_3 solid powders, the optical properties of both G-CGS/ZnS@Al_2O_3 and R-CIS/ZnS QDs@ Al_2O_3 and G-CGS/ZnS/Zr(i-PrO)$_4$@Al_2O_3 and R-CIS/ZnS/Zr(i-PrO)$_4$@Al_2O_3 QD hybrid powders were analyzed. As shown in Figs. 4 and 8, after producing powder QDs by drying and Al_2O_3 encapsulating process, the peak positions of PL spectra of the G-CGS/ZnS and R-CIS/ZnS QD samples are slightly or significantly red-shifted from solution to powder. This red-shift is mainly attributed to greater agglomeration of QDs during the solidification process following either the drying or encapsulating process of Al_2O_3. The PLEs of the G-CGS/ZnS and R-CIS/ZnS QD solid powders complexed by Zr(i-PrO)$_4$ are almost identical of those of the pristine G-CGS/ZnS and R-CIS/ZnS QD solid powders. However, the PLEs of the Al_2O_3- and Al_2O_3/Zr(i-PrO)$_4$-coated G-CGS/ZnS and R-CIS/ZnS QD samples are red-shifted from those of the QD solutions due to the agglomeration or increased size of QDs, resulting in an increased excitation intensity of blue light from a blue LED (Fig. 4 and Additional file 1: Fig. S6). The resulting Al_2O_3/Zr(i-PrO)$_4$-coated G-CGS/ZnS and R-CIS/ZnS QDs become more appropriate for use as color converters to convert blue to green and blue to red. As shown in Additional file 1: Fig. S6, like the small change of Zr(i-PrO)$_4$ complexed QDs in solutions, a slight alteration of the absorption of the Zr alkoxide complexed QDs is observed in the last Al_2O_3 powders. Strong absorption peaks below 400 nm for all powder samples suggest that the surfaces of the QDs are encapsulated with an oxide layer of Al_2O_3 or Al_2O_3/Zr(i-PrO)$_4$.

The outer Al_2O_3 coatings convert QD solution forms into ready-to-use QD powder forms. However, the Zr(i-PrO)$_4$ interlayer slightly blueshifts the peak wavelengths of both Al_2O_3-coated G-CGS/ZnS and R-CIS/ZnS QDs owing to the increase in distances among QDs (Fig. 8c, d, Table 2). In Table 2, it can be clearly seen that PLQYs improved slightly from 48.7 to 53.7% for green QDs and from 44.1 to 52.2% for red QDs after insertion of Zr(i-PrO)$_4$ interlayer between QD surfaces and Al_2O_3 outermost protective layer. The increase in PLQY can also suggest that the Al_2O_3 single layer coating likely plays a synergistic role in passivating and restoring QD defects formed by the Zr(i-PrO)$_4$ interlayer. However, for application to WLEDs, it is necessary to evaluate the effect of the Zr(i-PrO)$_4$ interlayer on the environmental stability of the outermost Al_2O_3 protective layer of the G-CGS/ZnS and R-CIS/ZnS QDs against UV, temperature, and moisture.

Here, to compare the stability of the Al_2O_3-coated and Al_2O_3/Zr(i-PrO)$_4$-coated G-CGS/ZnS and R-CIS/ZnS QDs, stability tests were performed on the solid powder form according to the phase of QDs obtained from fast hydrolysis reaction. As shown in Fig. 9, the temporal photo-stability, thermal-stability, and moisture-resistance of the solid-state forms of Al_2O_3-coated G-CGS/ZnS and R-CIS/ZnS QDs and Al_2O_3/Zr(i-PrO)$_4$-coated G-CGS/ZnS and R-CIS/ZnS QDs were

Table 2 Detailed optical properties of Al_2O_3 encapsulated CGS/ZnS based powder QDs and CIS/ZnS based powder QDs

Sample	Color coordinates		Peak wavelength (nm)	FWHM (nm)	PLQY (%)
	CIEx	CIEy			
CGS/ZnS@Al_2O_3	0.253	0.531	507	68	48.7
CGS/ZnS/Zr(i-PrO)$_4$@Al_2O_3	0.244	0.515	504	66	53.7
CIS/ZnS@Al_2O_3	0.607	0.384	621	90	44.1
CIS/ZnS/Zr(i-PrO)$_4$@Al_2O_3	0.588	0.403	611	93	52.2

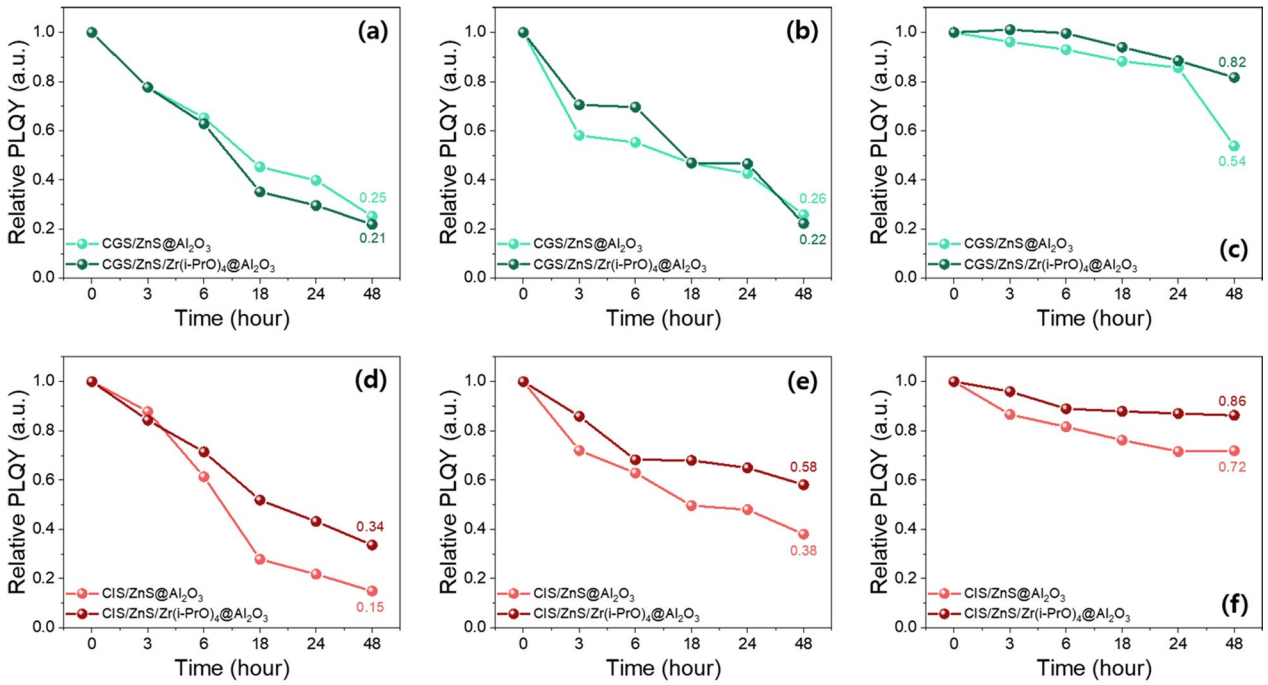

Fig. 9 **a** Photograph (under UV irradiation) and **b** thermal stability (120 °C heating condition) and **c** moisture resistance (under 85H/85T) of green Al_2O_3 encapsulated CGS/ZnS based QD hybrid powders. and **d** photograph and **e** thermal stability and **f** moisture resistance of red Al_2O_3 encapsulated CIS/ZnS based QD hybrid powders

tested under 365 nm UV irradiation, 120 °C heating condition, and 85% humidity/85 °C temperature (85H/85T) for a prolonged period. Because they are obtained as colloidal solutions, which cannot be transformed into solid forms, it is not reasonable to directly compare the stabilities of pristine and $Zr(i\text{-}PrO)_4$-complexed G-CGS/ZnS and R-CIS/ZnS QD solutions with those of solid forms of oxide-coated QDs. As shown in Fig. 9, both Al_2O_3-coated G-CGS/ZnS and R-CIS/ZnS QDs experienced moderate PLQY drops during UV irradiation, heat treatment, and moisture treatment of up to 50 h, retaining 25, 26, and 54% of original PLQYs of G QDs and 15, 38, and 72% of original PLQYs of R QDs. In the presence of a $Zr(i\text{-}PrO)_4$ interlayer, PLQY values of Al_2O_3-coated G-CGS/ZnS QD powders drop to 21, 22, and 82% after 50 h under heat, temperature, and moisture treatment, respectively. In the G-CGS/ZnS QDs, the stability is improved only under the 85H/85T condition; the interlayer has little effect on the stability under UV irradiation and heating conditions. On the other hand, in the case of R-CIS/ZnS QDs, the PLQY of $Al_2O_3/Zr(i\text{-}PrO)_4$-coated R-CIS/ZnS QD powders drops to 34, 58, and 86% after 50 h treatment of UV, heat, and moisture conditions, respectively. These graphs show that the stabilities of $Al_2O_3/Zr(i\text{-}PrO)_4$-coated QD powders are improved by the presence of a $Zr(i\text{-}PrO)_4$ interlayer under all UV, heat, and 85H/85T conditions. Although G-CGS/ZnS@Al_2O_3 QD powders are not improved under all conditions, the improvement of R-CIS/ZnS@Al_2O_3 QD powders under all conditions and G-CGS/ZnS Al_2O_3 QD hybrid powders under 85H/85T condition clearly show that an $Zr(i\text{-}PrO)_4$ interlayer is needed for further encapsulation process. The coating effect of the $Zr(i\text{-}PrO)_4$ interlayer of the $Al_2O_3/Zr(i\text{-}PrO)_4$ layer on the stability of G-CGS/ZnS is not so small compared with the encapsulating effect of the outermost Al_2O_3 coating layer. The significant enhancements in photo-stability, thermal-stability, and moisture-stability of the $Al_2O_3/Zr(i\text{-}PrO)_4$-coated R-CIS/ZnS samples clearly confirm that double $Al_2O_3/Zr(i\text{-}PrO)_4$-coatings are effective in passivating and protecting QD surfaces, as well as in forming solid state forms. To compare the effects of the $Zr(i\text{-}PrO)_4$ interlayer on the G-CGS/ZnS@Al_2O_3 and R-CIS/ZnS@Al_2O_3 QD powders in the DC-WLED package, two different WLED packages were fabricated by depositing Al_2O_3-coated G-CGS/ZnS and R-CIS/ZnS and $Al_2O_3/Zr(i\text{-}PrO)_4$-coated G-CGS/ZnS and R-CIS/ZnS QD powder pastes on blue LED cup-typed dies with two correlated color temperatures (CCTs) of 6500 K. At a current of 60 mA, the LE values of both Al_2O_3-coated QDs and $Al_2O_3/Zr(i\text{-}PrO)_4$-coated QD-based WLEDs

were found to be 40.44 and 63.2 lm/W in 6500 K. Regardless of the LE value, all four white LEDs showed high CRI values of 91 or 92 owing to the large FWHM (over 80 nm) of the G-CGS/ZnS and R-CIS/ZnS QDs. The comparison of LE values of WLEDs provides a direct comparison of the stability of the QD powders during fabrication of WLEDs filling the two different QD powder pastes in the LED cup-typed die. Figure 10 indicates that the LEs of the Al_2O_3/Zr(i-PrO)$_4$-coated I–III–VI QD-based WLEDs are improved 1.56 times compared to pristine Al_2O_3-coated G-CGS/ZnS and R-CIS/ZnS QD-based WLEDs, respectively.

These increases occurred because the Zr(i-PrO)$_4$ interlayer mitigates the degradation of both Al_2O_3-coated G-CGS/ZnS and R-CIS/ZnS QD powders during fabrication of DC-WLEDs. Based on the improved optical properties, it is clear that the G-CGS/ZnS/Zr(i-PrO)$_4$@Al_2O_3 and R-CIS/ZnS/Zr(i-PrO)$_4$@Al_2O_3 QD powders, synthesized by fast hydrolysis of Al(sec-BuO)$_3$ precursor and partially-induced hydrolysis of (Zr(i-PrO)$_4$) precursor, are suitable for application to DC-WLEDs with high CRI. Although the LEs of WLEDs incorporating were greatly improved by insertion of Zr(i-PrO)$_4$ interlayer, these LE values are still significantly smaller than those of commercially available DC-WLEDs, which use inorganic phosphors. In order to commercialize WLEDs using QD-embedded Al_2O_3 powders, additional protection materials and technology are required to minimize the degradation of optical properties of QDs during the harsh reaction needed to produce the QD-embedded oxide powders. Here, it is clearly seen that the introduction of a Zr(i-PrO)$_4$ passivation layer and interlayer improve the environmental stability of the eco-friendly I–III–VI QDs itself, and mitigates the further degradation of the I–III–VI QDs during additional inorganic layer coating and fabrication of WLED device.

Conclusion

The Zr(i-PrO)$_4$ complex was decorated on the surfaces of the G-CGS/ZnS and R-CIS/ZnS QDs to suppress ligand loss stemming from the secondary passivation layer. The PLQYs of the G-CGS/ZnS/Zr(i-PrO)$_4$ and R-CIS/ZnS Zr(i-PrO)$_4$ QD solutions reached similar values of ~ 95%. Their photostability and thermal stability were improved via surface oxidation, suppression of ligand loss, and Zr(i-PrO)$_4$ complex decoration-assisted QDs agglomeration. In addition, the Zr(i-PrO)$_4$ complex interlayer improves the optical properties of G-CGS/ZnS/Zr(i-PrO)$_4$@Al_2O_3 and R-CIS/ZnS/Zr(i-PrO)$_4$@Al_2O_3 QD hybrid powders during synthesis by fast hydrolysis of mixture solution of highly reactive Al(sec-BuO)$_3$ precursor and Zr(i-PrO)$_4$-decorated G-CGS/ZnS and R-CIS/ZnS QDs. Therefore, the PLQYs of the G-CGS/ZnS/Zr(i-PrO)$_4$@Al_2O_3 and R-CIS/ZnS/Zr(i-PrO)$_4$@Al_2O_3 QD hybrid powders reached 53.7 and 52.2% respectively, and material photostability and thermal stability also improved by surface oxidation, suppression of ligand loss, and Zr(i-PrO)$_4$ complex decoration-assisted QD agglomeration. The effect of Zr(i-PrO)$_4$ secondary passivation on the stability and PLQY values of the I–III–VI QDs and QD-embedded Al_2O_3 hybrid powders was studied by analyzing XRD, TEM, FT-IR, and XPS results to determine optical properties after coating of Zr(i-PrO)$_4$ on QDs and encapsulating Zr(i-PrO)$_4$-coated QDs with Al_2O_3 matrix. Finally, single WLED packages were fabricated using two sets of pristine GR QD@Al_2O_3 and GR Zr(i-PrO)$_4$-QD@Al_2O_3 QD hybrid powders. The LEs of the two WLEDs

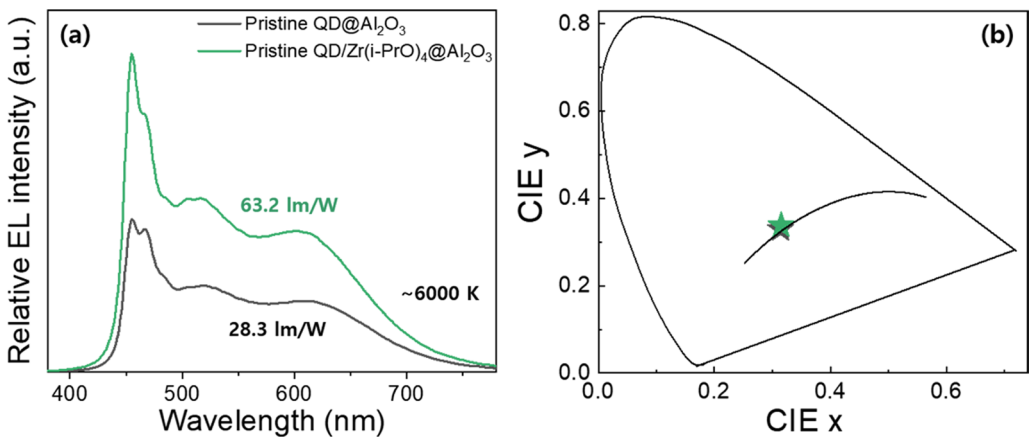

Fig. 10 **a** EL spectra and **b** CIE color coordinates of two correlated color temperatures (CCTs) of fabricated pristine QD@Al_2O_3 and pristine QD/Zr(i-PrO)$_4$@Al_2O_3 QD hybrid powders in DC-WLED package

implemented with G-CGS/ZnS/Zr(i-PrO)$_4$@Al_2O_3 and R-CIS/ZnS/Zr(i-PrO)$_4$@Al_2O_3 QD hybrid powders improved 2.25 and 2.40 times compared to those of cool and warm color WLEDs implemented with G-CGS/ZnS@Al_2O_3 and R-CIS/ZnS@Al_2O_3 QD hybrid powders, respectively. Although the currently developed I–III–VI /Zr(i-PrO)$_4$@Al_2O_3 QD hybrid powders cannot compete with commercialized inorganic phosphor powders, the introduction of a second passivation layer and interlayer of Zr(i-PrO)$_4$ provides a simple synthetic process to produce easy-to-use QD powders with improved optical properties for application to eco-friendly I–III–VI QD-based lighting and display devices.

Supplementary Information

The online version contains supplementary material available at https://doi.org/10.1186/s11671-022-03741-0.

Additional file 1. Supplementary figures.

Acknowledgements
Not applicable.

Author contributions
M. Ko and Y. R. Do designed the experiments and wrote the manuscript text. And M. Ko, S. Yoon and Y. Yang prepared I–III–VI QDs figures. Y. J. Eo analyzed XPS and FT-IR. K. N. Lee prepared Figs. 1, 6. All authors read and approved the final manuscript.

Funding
This work was supported by a National Research Foundation of Korea (NRF) grant funded by the Korea government (MSIT) (No. 2016R1A5A1012966, 2021R1A2C2009521) and the Ministry of Trade, Industry and Energy (MOTIE), Republic of Korea (No. 20016290).

Availability of data and materials
All data generated or analyzed during this study are included in this published article.

Declarations

Ethics approval and consent to participate
Not applicable.

Consent for publication
Not applicable.

Competing interests
The authors declare that they have no competing interests.

Received: 29 August 2022 Accepted: 20 October 2022
Published online: 07 November 2022

References

1. Chen B, Zhong H, Wang M, Liu R, Zou B (2013) Integration of $CuInS_2$-based nanocrystals for high efficiency and high colour rendering white light-emitting diodes. Nanoscale 5:3514–3519. https://doi.org/10.1039/C3NR33613A
2. Kim JH, Kim BY, Yang H (2018) Synthesis of Mn-doped $CuGaS_2$ quantum dots and their application as single downconverters for high-color rendering solid-state lighting devices. Opt Mater Express 8:221. https://doi.org/10.1364/OME.8.000221
3. Yoon HC, Oh JH, Ko M, Yoo H, Do YR (2015) Synthesis and characterization of green Zn-Ag-In-S and red Zn-Cu-In-S quantum dots for ultrahigh color quality of down-converted white LEDs. ACS Appl Mater Interfaces 7:7342–7350. https://doi.org/10.1021/acsami.5b00664
4. Yuan X, Ma R, Zhang W, Hua J, Meng X, Zhong X, Zhang J, Zhao J, Li H (2015) Dual emissive manganese and copper Co-Doped Zn-In-S quantum dots as a single color-converter for high color rendering white-light-emitting diodes. ACS Appl Mater Interfaces 7:8659–8666. https://doi.org/10.1021/acsami.5b00925
5. Jo DY, Yang H (2015) Spectral broadening of Cu–In–Zn–S quantum dot color converters for high color rendering white lighting device. J Lumin 166:227–232. https://doi.org/10.1016/j.jlumin.2015.05.043
6. Ko M, Yoon HC, Yoo H, Oh JH, Yang H, Do YR (2017) Highly efficient green Zn-Ag-In-S/Zn-In-S/ZnS QDs by a strong exothermic reaction for down-converted green and tripackage white LEDs. Adv Funct Mater 27:1602638. https://doi.org/10.1002/adfm.201602638
7. Ghosh S, Mandal S, Mukherjee S, De CK, Samanta T, Mandal M, Roy D, Mandal PK (2021) Near-unity photoluminescence quantum yield and highly suppressed blinking in a toxic-metal-free quantum dot. J Phys Chem Lett 12:1426. https://doi.org/10.1021/acs.jpclett.0c03519
8. Kim YH, Lee H, Kang SM, Bae BS (2019) Two-step-enhanced stability of quantum dots via silica and siloxane encapsulation for the long-term operation of light-emitting diodes. ACS Appl Mater Interfaces 11:22801. https://doi.org/10.1021/acsami.9b06987
9. Sheng Y, Tanga X, Xue J (2012) Synthesis of AIZS@SiO_2 core-shell nanoparticles for cellular imaging applications. J Mater Chem 22:1290. https://doi.org/10.1039/C1JM14794C
10. Moon H, Lee C, Lee W, Kim J, Chae H (2019) Stability of quantum dots, quantum dot films, and quantum dot light-emitting diodes for display applications. Adv Mater 31:1804294. https://doi.org/10.1002/adma.201804294
11. Jiang T, Shen M, Dai P, Wu M, Yu X, Li G, Xu X, Zeng H (2017) Cd-free Cu-Zn-In-S/ZnS quantum dots@SiO_2 multiple cores nanostructure: preparation and application for white LEDs. Nanotechnology 28:435702. https://doi.org/10.1088/1361-6258/aa878c
12. Liu Y, Li F, Huang H, Mao B, Liu Y, Kang Z (2020) Optoelectronic and photocatalytic properties of I-III-VI QDs: Bridging between traditional and emerging new QDs. J Semicond 41:091701. https://doi.org/10.1088/1674-4926/41/9/091701
13. Xu Y, Chen T, Xie Z, Jiang W, Wang L, Jiang W, Zhang X (2021) Highly efficient Cu-In-Zn-S/ZnS/PVP composites based white light-emitting diodes by surface modification. Chem Eng J 403:126372. https://doi.org/10.1016/j.cej.2020.126372
14. Rao P, Yao W, Li Z, Kong L, Zhang W, Li L (2015) Highly stable $CuInS_2$@ZnS: Al core@shell quantum dots: the role of aluminium self-passivation. Chem Commun 51:8757. https://doi.org/10.1039/c5cc01137j
15. Hu Z, Lu H, Zhou W, Wei J, Dai H, Liu H, Xiong Z, Xie F, Zhang W, Guo R (2023) Aqueous synthesis of 79% efficient AgInGaS/ZnS quantum dots for extremely high color rendering white light-emitting diodes. J Mater Sci Technol 134:189. https://doi.org/10.1016/j.jmst.2022.06.035
16. Wei J, Hu Z, Zhou W, Qiu Y, Dai H, Chen Y, Cui Z, Liu S, He H, Zhang W, Xie F, Guo R (2021) Emission tuning of highly efficient quaternary Ag-Cu-Ga-Se/ZnSe quantum dots for white light-emitting diodes. J Colloid Interface Sci 602:307. https://doi.org/10.1016/j.jcis.2021.05.110
17. Kim T, Yoon C, Song YG, Kim YJ, Lee K (2016) Thermal stabilities of cadmium selenide and cadmium-free quantum dots in quantum dot-silicon nanocomposites. J Lumin 177:54–58. https://doi.org/10.1016/j.jlumin.2016.04.038
18. Yoon SY, Kim JH, Jang EP, Lee SH, Jo DY, Kim Y, Do YR, Yang H (2019) Systematic and extensive emission tuning of highly efficient Cu-In-S-based quantum dots from visible to near infrared. Chem Mater 31:2627–2634. https://doi.org/10.1021/acs.chemmater.9b00550
19. Pan J, Shang Y, Bastiani MD, Peng W, Dursun I, Sinatra L, El-Zohry AM, Hedhili MN, Emwas AH, Mohammed OF, Ning Z, Bakr OM (2018) Bidentate ligand-passivated $CsPbI_3$ perovskite nanocrystals for stable near-unity photoluminescence quantum yield and efficient red light-emitting diode. J Am Chem Soc 140:562–565. https://doi.org/10.1021/jacs.7b10647

20. Li Z, Yao W, Kong L, Zhao Y, Li L (2015) General method for the synthesis of ultrastable core/shell quantum dots by aluminum doping. J Am Chem Soc 137:12430–12433. https://doi.org/10.1021/jacs.5b05462
21. Kim JH, Yang H (2014) White lighting device from composite films embedded with hydrophilic Cu(In, Ga)S_2/ZnS and hydrophobic InP/ZnS quantum dots. Nanotechnology 25:225601. https://doi.org/10.1088/0957-4484/25/22/225601
22. Kim JH, Jang EP, Kwon Y, Jang HS, Do YR, Yang H (2016) Enhanced fluorescent stability of copper indium sulfide quantum dots through incorporating aluminum into ZnS shell. J Alloys Compd 662:173–178. https://doi.org/10.1016/j.jallcom.2015.12.072
23. Jo JH, Kim MS, Han CY, Jang EP, Do YR, Yang H (2018) Effective surface passivation of multi-shelled InP quantum dots through a simple complexing with titanium species. Appl Surf Sci 428:906–911. https://doi.org/10.1016/j.apsusc.2017.09.125
24. Tepakidareekul M, Uematsu T, Torimoto T, Kuwabata S (2022) Encapsulation of $AgInS_2$/GaS_x core/shell quantum dots in-fumarate metal-organic frameworks for stability enhancement. CrystEngComm 24:3715–3723. https://doi.org/10.1039/D2CE00343K
25. Ahn SW, Ko M, Yoon S, Oh JH, Yang Y, Kim SH, Song JK, Do YR (2022) InP/ZnSeS/ZnS quantum dot-embedded alumina microbeads for color-by-blue displays. ACS Appl Nano Mater. https://doi.org/10.1021/acsanm.2c02638
26. Hu X, Gao X (2010) Silica-polymer dual layer-encapsulated quantum dots with remarkable stability. ACS Nano 4:6080–6086. https://doi.org/10.1021/nn1017044
27. Ow H, Larson DR, Srivastava M, Baird BA, Webb WW, Wiesner U (2005) Bright and stable core-shell fluorescent silica nanoparticles. Nano Lett 5:113. https://doi.org/10.1021/nl0482478
28. Ma Y, Li Y, Ma S, Zhong X (2014) Highly bright water-soluble silica coated quantum dots with excellent stability. J Mater Chem B 2:5043–5051. https://doi.org/10.1039/C4TB00458B
29. Nann T, Mulvaney P (2004) Single quantum dots in spherical silica particles. Angew Chem Int Ed 43:5393–5396. https://doi.org/10.1002/anie.200460752
30. Liu N, Yang P (2013) Highly luminescent hybrid SiO_2-coated CdTe quantum dots: synthesis and properties. Luminescence 28:542–550. https://doi.org/10.1002/bio.2491
31. Wang N, Koh S, Jeong BG, Lee D, Kim WD, Park K, Nam MK, Lee K, Kim Y, Lee BH, Lee K, Bae WK, Lee DC (2017) Highly luminescent silica-coated CdS/CdSe/CdS nanoparticles with strong chemical robustness and excellent thermal stability. Nanotechnology 28:185603. https://doi.org/10.1088/1361-6528/aa6828
32. Tang X, Chen W, Liu Z, Yao Z, Huang T, Chen C, Yang Z, Shi T, Hu W, Zang Z, Chen Y, Leng Y (2019) Ultrathin, core-shell structured SiO_2 coated Mn^{2+}-doped perovskite quantum dots for bright white light-emitting diodes. Small 15:1900484. https://doi.org/10.1002/smll.201970101
33. Jun S, Lee J, Jang E (2013) Highly luminescent and photostable quantum dot-silica monolith and its application to light-emitting diodes. ACS Nano 7:1472–1477. https://doi.org/10.1021/nn3052428
34. Huang S, Li Z, Kong L, Zhu N, Shan A, Li L (2016) Enhancing the stability of $CH_3NH_3PbBr_3$ quantum dots by embedding in silica spheres derived from tetramethyl orthosilicate in "Waterless" toluene. J Am Chem Soc 138:5749–5752. https://doi.org/10.1021/jacs.5b13101
35. Song WS, Kim JH, Yang H (2013) Silica-embedded quantum dots as downconverters of light-emitting diode and effect of silica on device operational stability. Mater Lett 111:104–107. https://doi.org/10.1016/j.matlet.2013.08.091
36. Wei J, Hu Z, Zhou W, Lu H, Zhang W, Guo R (2022) Color-converted white light-emitting diodes based on I–III–VI quantum dots: package strategies and stability promotion. Appl Mater Today 29:101585. https://doi.org/10.1016/j.apmt.2022.101585
37. Jang EP, Jo JH, Kim MS, Yoon SY, Lim SW, Kim J, Yang H (2018) Near-complete photoluminescence retention and improved stability of InP quantum dots after silica embedding for their application to on-chip-packaged light-emitting diodes. RSC Adv 8:10057–10063. https://doi.org/10.1039/C8RA00119G
38. Han CY, Jo JH, Yang H (2018) Towards the fluorescence retention and colloidal stability of InP quantum dots through surface treatment with zirconium propoxide. J Inf Display 19:143–149. https://doi.org/10.1080/15980316.2018.1498810
39. Li Z, Kong L, Huang S, Li L (2017) Highly luminescent and ultrastable $CsPbBr_3$ perovskite quantum dots incorporated into a silica/alumina monolith. Angew Chem Int Ed 56:8134–8138. https://doi.org/10.1002/anie.201703264

Publisher's Note

Springer Nature remains neutral with regard to jurisdictional claims in published maps and institutional affiliations.

Submit your manuscript to a SpringerOpen journal and benefit from:

- ► Convenient online submission
- ► Rigorous peer review
- ► Open access: articles freely available online
- ► High visibility within the field
- ► Retaining the copyright to your article

Submit your next manuscript at ► springeropen.com